

Ground-Based Remote Sensor Observations during PROBE in the Tropical Western Pacific



E. R. Westwater,* Y. Han,* J. B. Snider,* J. H. Churnside,+ J. A. Shaw,+ M. J. Falls,+
C. N. Long,# T. P. Ackerman,@ K. S. Gage,& W. Ecklund,** and A. Riddle**

ABSTRACT

From 6 January to 28 February 1993, the second phase of the Pilot Radiation Observation Experiment (PROBE) was conducted in Kavieng, Papua New Guinea. Routine data taken during PROBE included radiosondes released every 6 h and 915-MHz Wind Profiler–Radio Acoustic Sounding System (RASS) observations of winds and temperatures. In addition, a dual-channel Microwave Water Substance Radiometer (MWSR) at 23.87 and 31.65 GHz and a Fourier Transform Infrared Radiometer (FTIR) were operated. The FTIR operated between 500 and 2000 cm^{-1} and measured some of the first high spectral resolution (1 cm^{-1}) radiation data taken in the Tropics. The microwave radiometer provided continuous measurements within 30-s resolution of precipitable water vapor (PWV) and integrated cloud liquid, while the RASS measured virtual temperature profiles every 30 min. In addition, occasional lidar soundings of cloud-base heights were available. The MWSR and FTIR data taken during PROBE were compared with radiosonde data. Significant differences were noted between the MWSR and the radiosonde observations of PWV. The probability distribution of cloud liquid water was derived and is consistent with a lognormal distribution. During conditions that the MWSR did not indicate the presence of cloud liquid water, broadband long- and shortwave irradiance data were used to identify the presence of cirrus clouds or to confirm the presence of clear conditions. Comparisons are presented between measured and calculated radiance during clear conditions, using radiosonde data as input to a line-by-line Radiative Transfer Model. A case study is given of a drying event in which the PWV dropped from about 5.5 cm to a low of 3.8 cm during a 24-h period. The observations during the drying event are interpreted using PWV images obtained from data from the Defense Meteorological Satellite Program/Special Sensor Microwave/Imager and of horizontal flow measured by the wind profiler. The broadband irradiance data and the RASS soundings were also examined during the drying event.

*Cooperative Institute for Research in the Environmental Sciences, University of Colorado/NOAA, Environmental Technology Laboratory, Boulder, Colorado.

+NOAA/ERL/Environmental Technology Laboratory, Boulder, Colorado.

#Cooperative Institute for Research in the Environmental Sciences, University of Colorado/NOAA, Air Resources Laboratory, Boulder, Colorado.

@Department of Meteorology, The Pennsylvania State University, University Park, Pennsylvania.

&NOAA/ERL/Aeronomy Laboratory, Boulder, Colorado.

**Cooperative Institute for Research in the Environmental Sciences, University of Colorado/NOAA, Aeronomy Laboratory, Boulder, Colorado.

Corresponding author address: Dr. Ed R. Westwater, Cooperative Institute for Research in the Environmental Sciences, University of Colorado/NOAA, Environmental Technology Laboratory, 325 Broadway, MS R/E/ET1, Boulder, CO 80303-3328.

E-mail: ewestwater@etl.noaa.gov

In final form 19 August 1998.

1. Introduction

The tropical western Pacific (TWP) includes a large expanse of tropical ocean whose substantial variability has been associated with the El Niño–Southern Oscillation phenomenon. Several diagnostic studies have shown that the climatic variation in this region is associated with variability in other parts of the globe. Recent campaigns such as the Tropical Ocean and Global Atmosphere Coupled Ocean–Atmosphere Response Experiment (TOGA COARE) have been conducted in this region to gather, distribute, and analyze basic oceanic, atmospheric, and radiation data. As a part of the U.S. Department of Energy’s Atmospheric Radiation Measurement (ARM) program (Stokes and Schwartz 1994), as many as five Atmospheric Radiation and Cloud Stations (ARCS) will

be deployed in the TWP. An ARCS consists of an integrated set of instruments to measure the surface radiation balance, surface meteorological parameters, cloud properties, and limited atmospheric quantities. This paper describes data taken during an experiment that was a prototype for the ARCS deployment (Long et al. 1994) and was also a part of TOGA COARE (Webster and Lucas 1992).

From 6 January to 28 February 1993, the National Oceanic and Atmospheric Administration's Environmental Technology Laboratory (ETL) and Aeronomy Laboratory (AL), The Pennsylvania State University, the Commonwealth Scientific and Industrial Research Organization (CSIRO), and the National Center for Atmospheric Research (NCAR) participated in the Pilot Radiation Observation Experiment (PROBE) in Kavieng, New Ireland Province, Papua New Guinea (PNG). Kavieng ($2^{\circ}34'S$, $150^{\circ}48'E$) is at the tip of the narrow island expanse of New Ireland and has a roughly 180° sector of open ocean to the northeast (see Fig. 1). The instruments at Kavieng were located at the local airport and weather station. Further details about PROBE are given by Renné et al. (1994) and Long et al. (1994).

Data taken by the NCAR/AL's Integrated Sounding System (ISS) (Parsons et al. 1994) during PROBE included radiosondes, 915-MHz Wind Profiler–Radio Acoustic Sounding System (RASS) observations of winds and temperatures, and surface meteorological observations. The radiosondes used the Cross-chain Loran Atmospheric Sounding System (CLASS)-type NAVOID (Loran–Omega) sounding system. Lidar measurements of cloud-base heights and, for cirrus clouds, thicknesses were taken by a lidar operated by CSIRO (Platt et al. 1998). In addition, ETL operated

a dual-channel Microwave Water Substance Radiometer (MWSR) at 23.87 and 31.65 GHz and a Fourier Transform Infrared Radiometer (FTIR). The FTIR operated between 500 and 2000 cm^{-1} and provided some of the first high-spectral resolution (1 cm^{-1}) radiation data taken in the Tropics. The microwave radiometer provided continuous measurements with 30-s resolution of precipitable water vapor (PWV) and integrated cloud liquid (ICL), the RASS measured virtual temperature profiles every 30 min, and the cloud lidar provided episodic measurements of clouds every minute. The remote sensing data, the CLASS data, and extensive in situ radiation data provide information that will be extremely valuable to climate models. In addition, the performance of key instruments in a very hostile environment were addressed—a prerequisite for the ARCS long-term development. Among the key questions to be addressed with these data are the following: 1) what is the accuracy of such remote-sensing measurements in a tropical environment; 2) what is the magnitude of the water-vapor continuum absorption; and 3) what are the temporal and frequency distributions of cloud liquid and how do they differ from those at temperature latitudes?

2. Description of equipment

a. Dual-frequency Microwave Water Substance Radiometer (MWSR)

The MWSR is a refinement of a system described by Hogg et al. (1983). In addition to electronics upgrades, this instrument differed from earlier versions by operating the lower-frequency channel at 23.87 GHz rather than 20.6 GHz. Both generations of instruments were designed to run continuously and to provide unattended operations in almost all weather conditions. The salient characteristics of the new instrument are shown in Table 1. The internal gain calibration of the radiometers is done by switching between the antenna and two temperature-controlled blackbody loads; during clear skies, external calibration was done using the “tip cal” method (Han et al. 1994). In contrast to our experiences in nontropical environments, cloudy periods were the norm rather than the exception, and thus relatively few tip cals were performed during PROBE.

The observed brightness temperature T_b at the two frequencies is sensitive to columnar amounts of water vapor and cloud liquid. From two measurements of T_b , we derive precipitable water vapor and integrated cloud liquid every 30 s (or in some cases, every two min) using linear a priori statistical inversion

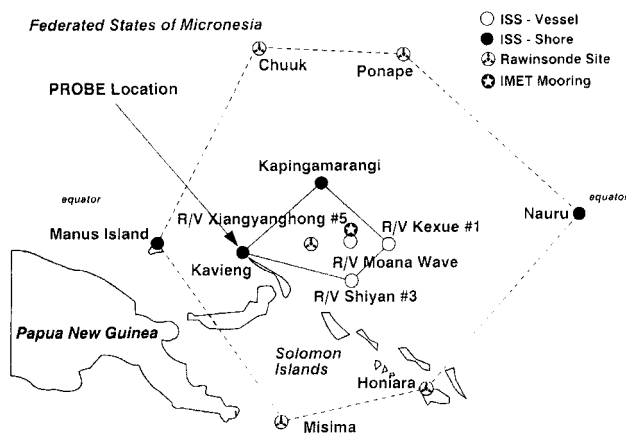


FIG. 1. Location of PROBE during TOGA COARE. The solid lines delineate the Intensive Flux Array and are within the overall TOGA COARE study area.

TABLE 1. Characteristics of the ETL dual-channel MWSR used in PROBE.

Operating frequencies	23.87 and 31.65 GHz
Viewing	Zenith
Antenna half-power beamwidth	5.0
Bandpass (double side band)	40–250 MHz
Integration time	30 s
Sensitivity (for 30 s)	0.1 K rms
Absolute accuracy	0.75 K

(Westwater 1993). Our a priori dataset was developed from CLASS radiosonde observations that were obtained during phase one and the first 13 days of phase two of PROBE. The a priori data and the set to which we compare our data are nonintersecting. A total of 336 radiosondes was contained in the a priori ensemble. The accuracy of our PWV retrievals is insensitive to the details of the statistical ensemble, but depends strongly on the accuracy of calibration and the accuracy of the “forward model” used in constructing retrieval coefficients. We used Liebe’s 1987 millimeter-wave propagation model (Liebe and Layton 1987; Liebe 1989) in modeling our data. In contrast to Han et al. (1994), we made no empirical adjustment between measured and calculated brightness temperatures in our retrievals of vapor.

b. Fourier Transform Infrared Radiometer (FTIR)

The FTIR developed by ETL (Shaw et al. 1991) is a simple, ground-based Fourier transform spectrometer–radiometer. It is based on a compact and rugged Michelson interferometer, operating between roughly 500 and 2000 cm^{-1} (5.0–20.0 μm) with 1 cm^{-1} spectral resolution. Downwelling atmospheric emission in the entire bandwidth is viewed simultaneously with a single liquid nitrogen (LN₂)-cooled HgCdTe detector. A fast Fourier transform of the measured interferogram then yields the emission power spectrum. We view two black-body calibration targets immediately before and after each complete atmospheric emission measurement. Collection of each spectrum takes about 1 s, and we average 100 such spectra to reduce random noise. With this technique, calibrated atmospheric spectra are collected about once every 6–10 min.

To compare the calibrated radiance spectra with theory, we use radiosonde observations of temperature, water vapor, and pressure, and insert these observations into a radiative transfer model. At the time of these measurements, the best radiative transfer model available used the CKD_1 continuum model (Clough et al. 1989) with the line-by-line Radiative Transfer Model (LBLRTM) (Clough et al. 1992) that now has the new CKD_2.2 continuum (Han et al. 1997). For the current application LBLRTM has three relevant features: it has been and continues to be extensively validated against atmospheric radiance spectra; it incorporates a full water vapor continuum model; and its computational efficiency mitigates the computational burden of the line-by-line calculation for retrieval studies over extended spectral domains.

c. Wind profiler–Radio Acoustic Sounding System (RASS)

The wind profiler–RASS used in PROBE is described by Parsons et al. (1994) and Carter et al. (1995). The accuracies of these data have been analyzed by Riddle et al. (1996) who compared both in situ versus profiler-derived winds and in situ versus RASS-derived virtual temperatures for the TOGA COARE period. For our purposes, we note that the temporal resolution of the system was 30 min, the vertical resolutions of the wind profiler for low/high modes were 100 and 400 m, and the vertical resolution of RASS was 60 m.

d. Ancillary observations

In addition to the radiometric observations, ETL also took surface meteorological observations of temperature, pressure, and relative humidity. Simultaneously, NCAR obtained surface observations, and NCAR-trained weather observers launched CLASS radiosondes every 6 h. Radiation measurements included upwelling and downwelling longwave irradiance, downwelling and upwelling shortwave irradiance, and diffuse and direct shortwave downwelling irradiance. The shortwave irradiance measurements were useful in determining clear and cloudy conditions (Long 1996; Long and Ackerman 1996).

3. Observations

a. MWSR

The MWSR operated continuously through PROBE and, except for periods of rain, the data ap-

pear to be of high quality. After initial deployment, skies were cloudy and the number of tip calcs was quite limited. In this paper, we analyze data from 14 January through 28 February 1993 because of uncertainties in the initial calibration and antenna alignment. We show in Fig. 2 a 48-h time series of PWV and ICL derived from the MWSR; also shown by the large dots are the values of PWV derived by integrating the CLASS radiosonde humidity profiles. These spikes in the data show the occurrence of clouds and some rain during this period and we see good agreement between MWSR and CLASS measurements of PWV. In this example, there was only a small variation in PWV from about 5.0 to 5.5 cm. During PROBE, the PWV varied from 3.8 to 7.0 cm. In contrast, over a year in Denver, Colorado, where we have taken several years of observations, PWV has varied from 0.5 to 3.5 cm.

During the time subsequent to PROBE, it was discovered that corrections were necessary for low-level temperature and humidity profiles measured by the CLASS radiosondes. As discussed by Cole and Miller (1995), errors occurred because of two causes: solar heating and sensor lag. All of the radiosondes that we analyze in this paper have been reprocessed by NCAR, and the Cole–Miller corrections have been applied.

We show in Fig. 3 a continuous time series of all of PWV data that were measured by the MWSR and the 6-hourly radiosonde data. For effectiveness in presentation, the period 14–19 January 1993 is not shown, although the quality of the data is similar to that of the next 10 days. These time series have been quality controlled by rejecting data for which the inferred integrated liquid water is greater than 3 mm [$T_b(31.65 \text{ GHz}) < \sim 135 \text{ K}$] and a three-point median filter was subsequently applied. Generally

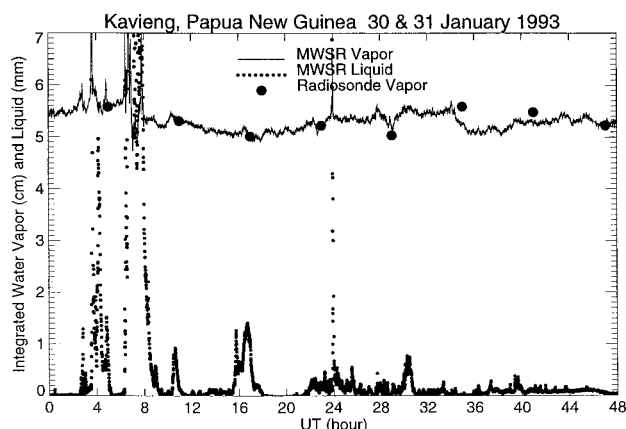


FIG. 2. A 48-h time series of PWV and ICL derived from the MWSR. Kavieng, PNG, 30–31 January 1993 UTC. The large dots are PWV values derived from CLASS radiosondes.

speaking, there were long periods during which there was excellent agreement between MWSR and radiosonde data: from 14 January to 5 February (Julian days 14 to 36), from 10 to 17 February (Julian days 41 to 48), from 27 to 28 February (Julian days 58 to 59), and intermediate periods where the agreement was poor. Poor agreement between radiometers and radiosondes frequently occurs when there are sharp horizontal gradients in water vapor accompanied by moderate winds or when rain can adversely affect radiometers. Such data were occasionally present in our time series but are easily identified. The more troublesome data appear as consistent biases between the radiosonde and the radiometer, such as are readily apparent from 20 to 25 February (Julian days 51 to 56). Among the possible radiometric causes that we investigated to explain such anomalies included calibration drifts in either or both channels. We checked for such calibration drifts by 1) comparing tip cal data throughout the experiment and 2) statistical variance analysis, done on a daily basis, of internal calibration data.

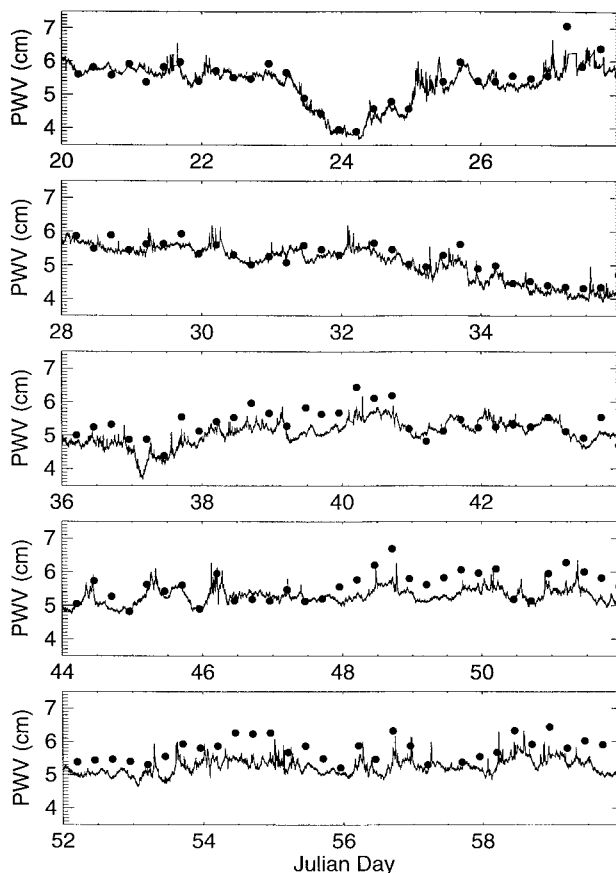


FIG. 3. Time series of PWV, derived from MWSR and CLASS radiosondes. Kavieng, PNG, 20 January–28 February 1993. The large dots are PWV values derived from CLASS radiosondes. Times are in Julian day (UTC).

We also looked for diurnal effects, but none were present. Finally, we developed and applied to the data three physically based quality control (QC) procedures (in addition to the three-point median filter and, in the case of PWV retrievals, of restricting ICL to being less than 3 mm). The first is based on theoretical relationships that exist between 23.87- and 31.65-GHz brightness temperatures. Using the a priori data, we calculated T_b values to represent the expected range of values that could occur for this climatology; a reasonable range of clouds and cloud liquid amounts were contained in these calculations. From scatterplots of these theoretical values, a border region was determined such that measured data falling outside of the border region were rejected. Figure 4 shows these borders as well as measured points. We note some rejected points below the lower straight-line boundary showing data slightly out of calibration; we also observe rain effects when rejecting some data for which 23.87-GHz T_b values are greater than about 200 K. We use the physical border method again when screening the data for outliers in determining ICL (see section 3f). The second method of QC was based on theoretical values of the ratio of the derived water vapor absorption at the two frequencies during clear conditions; we chose a liquid threshold of 0.04 mm as indicating clear conditions. During daytime, we also used clear times as determined by total hemispheric and diffuse solar irradiance observations following the method developed by Long (1996). For the clear periods, we computed

$$R = \frac{\tau_{23.87} - \tau_{d23.87}}{\tau_{31.65} - \tau_{d31.65}},$$

where τ and τ_d refer to derived total and computed dry attenuation at the indicated frequency (GHz). Using calculations based on the a priori database, the theoretical values of R varied over the range 2.60 to 3.05; data whose values were outside of this range were

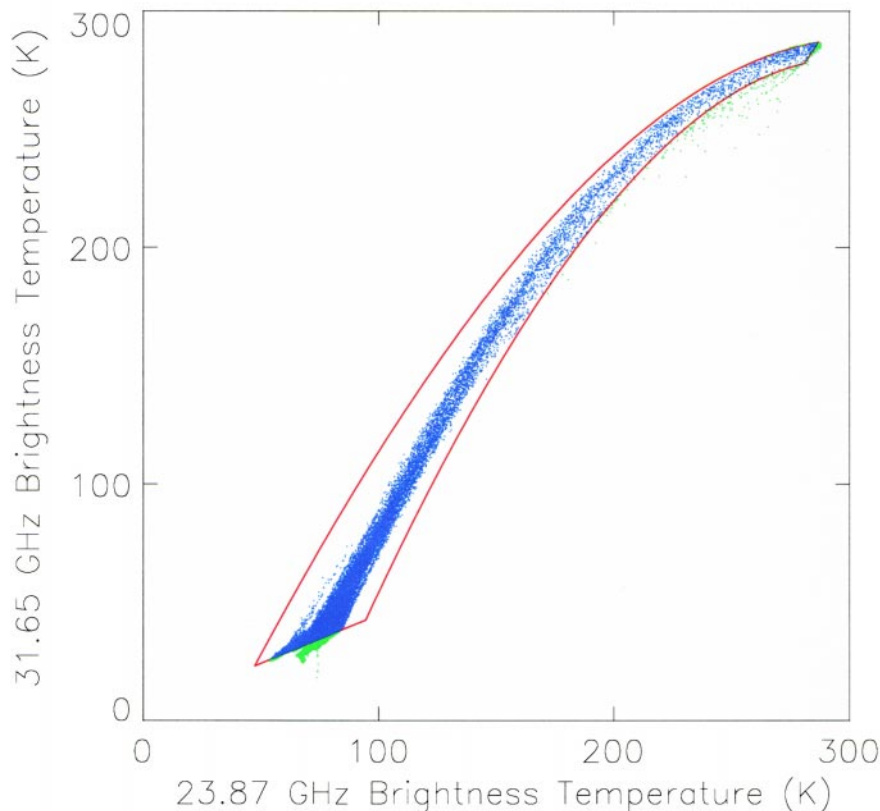


FIG. 4. Quality control region for Kavieng, PNG, brightness temperature data (red curve) and measured data. Data passing this quality control are shown in blue ($n = 116\,981$), and data outside of quality control are shown in green ($n = 11\,812$).

omitted. Finally, we also eliminated data when the changes in inferred PWV exceeded 2 mm min^{-1} . This latter criterion was used to eliminate rain and cloud effects on timescales less than our 30-s averaging period. About 3% of all data used to infer PWV were rejected by these methods.

Even after applying all of the above radiometric quality control methods, it was apparent that substantial discrepancies remained between radiometer and radiosonde. In investigating possible sources of radiosonde error, we also compared ETL's surface observations with those provided by ISS. No change in the overall character of the time series was observed. However, research reported by Liljegren and Lesht (1996) showed that substantial differences between Vaisala RS-80 radiosondes with H-Humicap relative humidity sensors occurred between radiosondes that were obtained from different calibration lots, that is, batches of radiosondes that were calibrated at different times. Unfortunately, the radiosonde identification information was not kept during the PROBE experiment, so that further examination of this likely cause of problems was not possible. However, our analysis of

the radiometer data showed no calibration shifts during the course of the experiment. Thus, without any clear-cut criteria to reject additional radiometric or radiosonde data, we kept and present all of the radiosonde data but used caution when calculating infrared spectra during periods when radiosondes differed substantially from the MWSR.

We show in Fig. 5 a scatterplot comparison of PWV as measured by the MWSR and by radiosondes. As we have seen in Fig. 3, data taken before 6 February agreed well with radiosondes, while those taken after this date, for the most part, do not agree as well. To show this, we plot the data from the earlier period in circles and the later data in triangles. The statistical comparisons shown in the upper-right and lower-left portions of the plots reflect these substantial differences. For example, the average difference in PWV (i.e., the bias) is more than a factor of 4 greater in the latter period. For completeness, we summarize the separate and composite results in Table 2. Even ignoring the differences between data from the two time periods, the data are in much better agreement with collocated radiosonde data than similar PWV retrievals obtained from Defense Meteorological Satellite Program/Special Sensor Microwave/Imager (SSM/I) data (Sheu and Liu 1995). Our composite rms difference of 0.373 cm is somewhat higher than values that ETL has achieved previously. For example, for a year

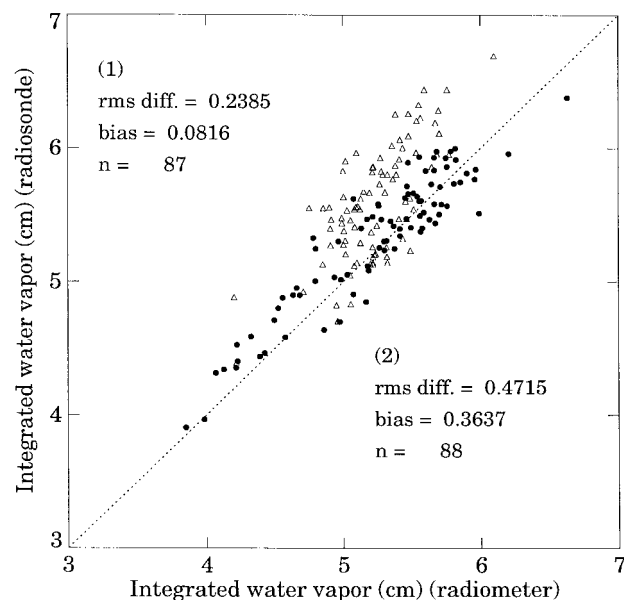


FIG. 5. Scatterplot of PWVs derived from MWSR and CLASS radiosondes, Kavieng, PNG, 14 January–28 February 1993. The circles and statistics (2) refer to data taken before 6 February, while the triangles and statistics (1) refer to subsequent data.

TABLE 2. Statistical comparisons of radiometric retrievals of PWV (cm) and radiosondes for the period 14 January–28 February 1993 at Kavieng, Papua New Guinea. For the regression analysis, PWV from the MWSR is the independent variable.

	14 Jan– 5 Feb	6–28 Feb	14 Jan– 8 Feb
Rms difference (cm)	0.239	0.472	0.373
Bias (sonde–MWSR)	0.082	0.364	0.223
Intercept (cm)	0.692	0.200	0.712
Slope	0.884	1.031	0.907
Est. std dev (cm)	0.217	0.303	0.299
Sample size	87	88	175

of operational data at Denver, Colorado, rms differences of 0.17 cm were achieved (Westwater 1993); for a research comparison with Raman lidar, an rms difference of 0.03 cm was achieved (Han et al. 1994). Typical rms differences achieved by SSM/I sensors over tropical oceans during TOGA COARE ranged from 0.50 to 0.95 cm, and depended on the type of retrieval algorithm used (Sheu and Liu 1995). However, our data suggest that at least some component of the satellite differences may be due to radiosonde error.

b. MWSR and SSM/I observations of a drying event

During most of our observations in Kavieng, the PWV exhibited small changes during the course of a day and with a range mostly confined from 5.0 to 6.5 cm. However, a notable exception occurred during a 60-h period that started at 1800 UTC 22 January and extended until 0600 UTC 25 January (see Fig. 3). During the initial 12-h period, changes in PWV of only a few millimeters occurred, but between 0600 UTC 23 January until 0000 UTC 24 January a steady drop in vapor was observed. For about 6 h, the PWV remained at around 4 cm, and then the vapor slowly increased until it reached a 5.5-cm value of 0100 UTC 25 January, and clouds and rain were subsequently observed. Representative radiosonde soundings from this period are shown in Fig. 6. The initial sounding on 1654 UTC 22 January 1993 shows a humidity profile that is within a few degrees of saturation throughout most of the troposphere. However, starting at 0459 UTC 23 January 1993 (not shown), a low-level drying began

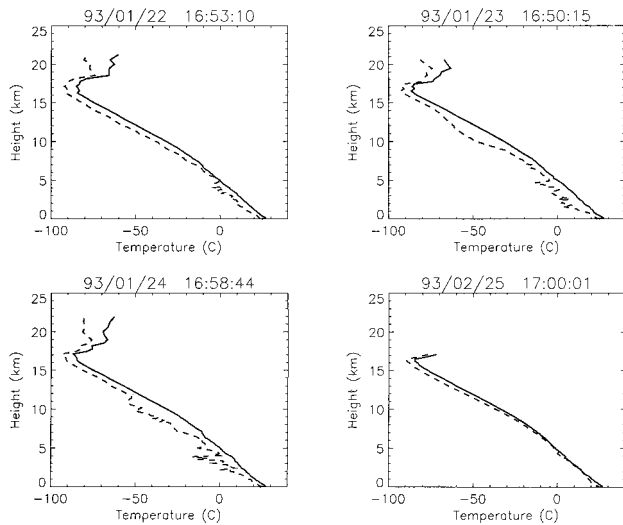


FIG. 6. 1700 UTC radiosonde soundings at Kavieng, PNG, 22–25 January 1993.

and, by 1653 UTC 23 January 1993, extended through most of the troposphere. The dry atmosphere was still present on 1700 UTC 24 January. Finally, by the sound-

ing of 0500 UTC 25 January, the moisture was again approaching saturation throughout the troposphere. What kind of atmospheric flow could have caused this behavior?

An initial suggestion for the sudden drying was that a dry air mass from Australia could have been carried over Papua New Guinea. However, observations from the wind profiler at Kavieng showed that the winds were coming from the open ocean to the east and were basically steady in direction from 1800 UTC 21 January to 1000 UTC 24 January. For our analysis, the important point is that during the drying on 23 January, the winds were steady. Thus, if the moisture suffered a substantial decrease and the winds were steady, then there had to be substantial horizontal gradients in the moisture field.

To investigate the presence, if any, of horizontal moisture gradients, we were able to obtain composite PWV images from SSM/I data (see Fig. 7). The details of processing of these data are given by Sheu and Liu (1995); each of the images in Fig. 7 is derived from a composite of four to five SSM/I sampling swaths,

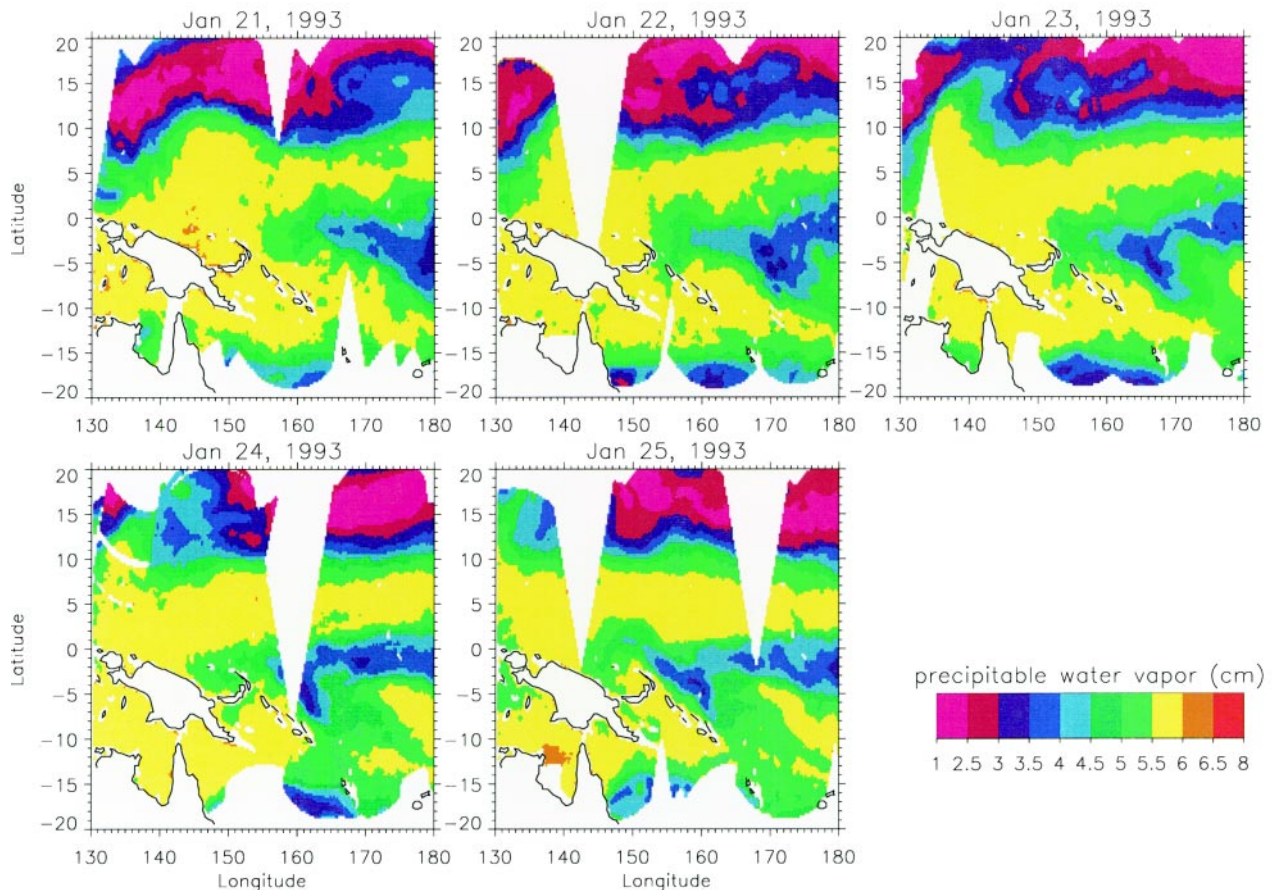


FIG. 7. Images of PWV (cm) derived from the SSM/I from 21 to 25 January 1993 over the tropical western Pacific.

each of which is separated in time by 102 min. As is evident, the PWV images derived from SSM/I brightness temperatures show substantial horizontal gradients. On 21 January, Kavieng is immersed in a moist air mass of from 5.5 to 6.0 cm of PWV. On 22 January, a much drier air mass is approaching, and by 24 January, the dry region surrounds all of the New Ireland region, including Kavieng. Finally, on 25 January, Kavieng is again moist, although there are very sharp horizontal gradients in the PWV field to the northeast. Thus, remembering that the satellite images were derived from basically one day's data, the qualitative agreement between the MWSR and SSM/I is excellent.

The causes of such drying events were discussed by Sheu and Liu (1995). Basically, they showed that anomalous wind regimes (westerly wind bursts) were responsible for the transport of dry air from the subtropics into the TOGA COARE domain. Reestablishment of the easterlies brings the PWV field back to its normally high values. The establishment and operation of the continuously operating five-station ARCS observing network may be able to capture more of these interesting and, perhaps, significant events.

c. Shortwave and longwave observations during the dry event

The PROBE surface downwellings shortwave (SW) and IR (longwave) are shown in Fig. 8 for the period from 1200 UTC 20 January through 1200 UTC 26 January. Manufacturer uncertainty estimates for these data are about 3% or 15 W m^{-2} (Long 1996). From the PWV time series in Fig. 3, it is apparent that the dry front inclusion over Kavieng was greatest from roughly 1200 UTC on 23 January through 1200 UTC 24 January (defined as "dry"). From the time series of downwelling SW in Fig. 8, this period also appears to

have been less cloudy. Daily averages are taken from 1200 to 1200 UTC so that each 24-h average includes a complete solar diurnal cycle. Defining "normal" as the period from 1200 UTC 20 January through 1200 UTC 26 January and excluding the dry 24-h period noted above, a comparison of the surface radiative energy differences is possible. Table 3 gives the normal and dry averages of the various components measured during this period. The 24-h average net SW increases by about 66 W m^{-2} during the dry front episode while the net IR decreases from -47 to -71 W m^{-2} , a change of 24 W m^{-2} . Thus, the net radiative energy input into the surface increases by about 42 W m^{-2} , or 45% of the normal net irradiance, on a 24-h basis during a dry episode compared with more normal conditions encountered during PROBE.

Clear-sky (i.e., cloudless) surface downwelling SW irradiances were calculated using a delta two-stream model incorporating the numerical scheme of Toon et al. (1989) and a solar ephemeris algorithm developed by Wilson (1980). The IR irradiances were calculated using the MODTRAN code (Berk et al. 1989). Model inputs include an aerosol size distribution obtained from sun photometer measurements obtained during PROBE, the Air Force Geophysics Laboratory Tropical Ozone profile, and temperature, pressure, and water vapor profiles from radiosondes launched at Kavieng (Long 1996). Uncertainty estimates for these data are roughly equal to that for the measurements, with clear-sky comparisons between model calculations and measurements having rms deviations from perfect agreement of about 10 W m^{-2} (Long 1996). The results of these calculations are shown in Fig. 8 and listed in Table 3.

The cloud effect on downwelling irradiances is measured by the difference between the irradiance incident on the surface and that which would be expected under cloudless conditions, in this case from the model results. Negative values denote a decrease in energy input at the surface due to the presence of clouds. The magnitude of the 24-h average SW cloud effect decreases by roughly 87 W m^{-2} during the dry episode compared to a 9 W m^{-2} change in the IR cloud effect (Table 3). Due to the large column concentration of water vapor, the tropical atmosphere is nearly opaque across the thermal infrared spectrum; consequently, only small

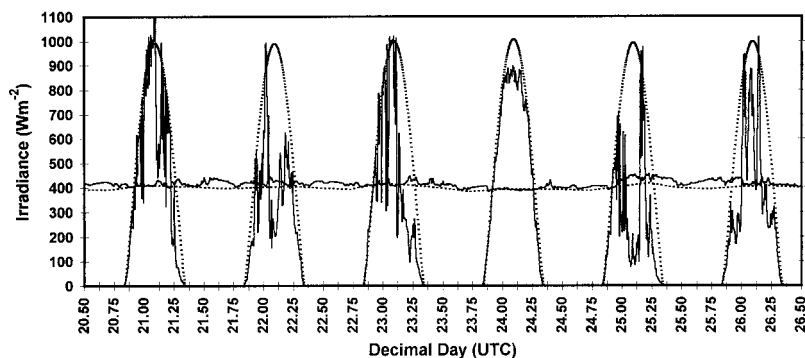


FIG. 8. Measured surface downwelling SW (heavy solid) and IR (thin solid) and clear-sky (model) downwelling SW (heavy dashed) and IR (thin dashed) from PROBE.

TABLE 3. Twenty-four-hour averages of PROBE radiative energy budget components (in W m^{-2}) and surface albedo from 1200 UTC 20 January through 1200 UTC 21 January.

	Normal	Dry
Downwelling SW	185.1	274.5
Upwelling SW	45.5	69.3
Downwelling IR	419.1	398.6
Upwelling IR	466.2	469.7
Net radiation	92.4	134.1
Model downwelling SW	304.6	306.9
SW cloud effect	-119.6	-32.4
Model downwelling IR	401.1	390.1
IR cloud effect	18.0	8.5
Total cloud effect	-101.6	-23.9
SW direct component	72.0	168.7
SW diffuse component	113.1	105.8
Surface albedo	24.9%	26.2%

variations in the downwelling IR occur (Fig. 8). The effect of clouds is much more apparent in the downwelling SW. The smaller value of the SW cloud effect during the dry episode (Table 3) confirms that this 24-h period was less cloudy than the surrounding days. Another indication of the decrease in cloudiness comes from an examination of the direct and diffuse components of the downwelling SW measured during this period. The normal 24-h averages of 113 and 72 W m^{-2} for the diffuse and direct components, respectively, indicate that more of the downwelling SW energy at the surface comes from the diffuse component, as is expected for frequently cloudy conditions (Table 3). Measurements from the entire 4-month duration of PROBE (November 1992–February 1993) show that on average over half (53%) of the incident SW comes from the diffuse component (Long 1996). During the dry episode, however, the direct component increased by about 97 W m^{-2} while the diffuse component decreased by about 7 W m^{-2} . This net 90 W m^{-2} increase in total downwelling SW during the

dry episode is primarily due to less cloudy conditions allowing more of the direct solar irradiances to reach the surface. The surface albedo exhibits a slight relative increase (about 1%) during these less cloudy conditions (Table 3), when the downwelling irradiance is less isotropic; that is, more peaked in the direction of the sun. However, since the albedo is determined using a downward-facing pyranometer over the PROBE site land surface at a height of 1 m, the absolute accuracy of the albedo measurements is no better than about 5%.

One characteristic of the dry episode was the decrease in cloudiness, and this decrease, in turn, can be related to the decrease in water vapor. Figure 9 shows a time series of the calculated convective available potential energy (CAPE) (based on the dry-bulb temperature profile and lifting of the lowest 50-mb layer) from Kavieng radiosonde data obtained during the period. As the atmospheric profile becomes drier, a significant decrease in CAPE occurs until moistening aloft reoccurs. Thus, while the decrease in PWV has little effect on the clear-sky surface radiative energy budget, the connection to larger-scale forcings indicated by the dry episode has a much more pronounced effect on the actual energy budget due to an attendant decrease in cloud production.

For our selected 6-day period, we show cloud fraction in Fig. 10, along with a time series of upwelling SW and IR at the tropopause representative of the TOGA COARE Intensive Flux Array area (Webster and Lucas 1992). Kavieng was the westernmost corner of this array. These values are calculated from International Satellite Cloud Climatology Project (ISCCP) data products that are derived from *GMS-4* satellite measurements obtained during TOGA

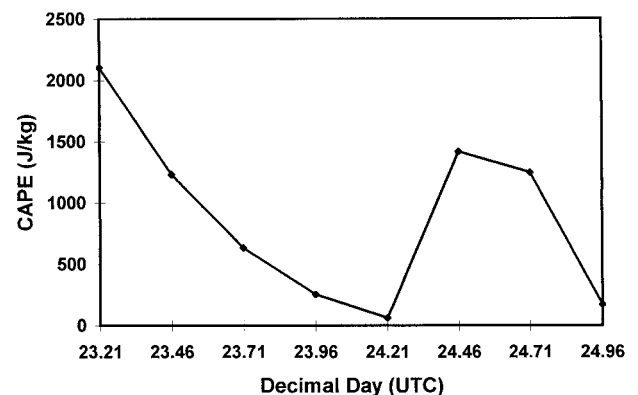


FIG. 9. CAPE calculated from CLASS soundings using the dry-bulb temperature profile and lifting of a 50-mb layer near the surface.

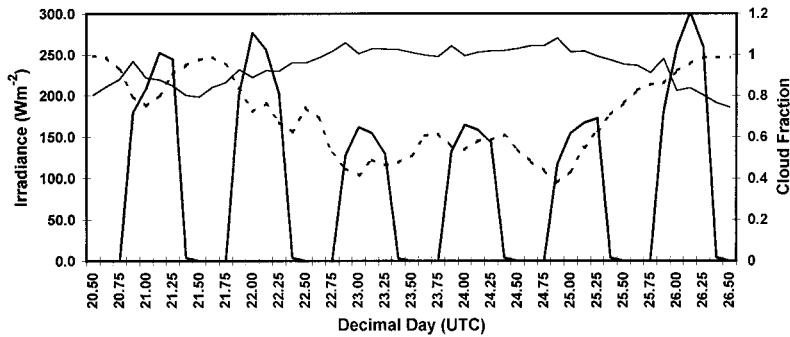


FIG. 10. ISCCP top-of-the-atmosphere upwelling SW (heavy solid), upwelling IR (thin solid), and cloud fraction (dashed) for the TOGA COARE IFA area (adjusted to tropopause values).

COARE. For this large area, the dry episode lasted from 1200 UTC 22 January to 1200 UTC on 25 January (based on 24-h averages). Defining these three days as dry for the IFA and the remaining three days as normal, then the average cloud fraction decreases from about 87% for normal conditions to about 54% during the dry episode. The normal average upwelling irradiance for the period is 118 W m^{-2} in the SW and 219 W m^{-2} in the IR. The upwelling SW decreases by 43 W m^{-2} during the dry period due to the decrease in upward reflection from clouds, while the upwelling IR increases by 35 W m^{-2} . Thus at the tropopause, unlike at the surface, the changes in the SW and IR components nearly offset each other, resulting in a net increase of only about 8 W m^{-2} into the system during the dry episode.

d. RASS observations during the dry event

RASS operated continuously during PROBE and provided data every 30 min; the data may be used to study boundary layer dynamics and also possibly used as input to profile retrieval algorithms (Han and Westwater 1995). An assessment of RASS accuracy in a tropical environment is given by Riddle et al. (1996). They also discuss the initial quality control that is provided by the ISS system and the various quality flags that are attached to each profile. Vertical velocity corrections are made to the data during clear air situations, since they improve the accuracy but are not made when hydrometers are present, since they degrade

the accuracy (Angevine et al. 1994). However, even after first-order quality control, plots of RASS data revealed many outliers, especially during convective conditions. We applied an additional quality control method that used information on both signal strength and observations of cloud liquid from the MWSR. On strictly quality controlled data, we compared the differences between RASS- and radiosonde-measured virtual temperature T_v as a function of altitude. In the first 500 m above ground

level (AGL), the RASS measurements were significantly colder than those of the radiosonde. Above 500 m, the biases diminished and the rms differences approached previously established accuracies (0.5 K) of the RASS instrument (May et al. 1990). At present, the source of the lower-altitude differences is not clear, but as shown by Riddle et al. (1996), the differences occurred at all of the five ISS sites during TOGA COARE.

We also derived continuous profiles of T_v from RASS by filling in missing points eliminated by quality control. Our method to reinsert points used both spatial and temporal interpolation of the RASS data and also corrected the data for the biases. After these corrections, there was agreement to about $\pm 0.5^\circ\text{C}$ with the radiosonde data. In Fig. 11, we show the time-

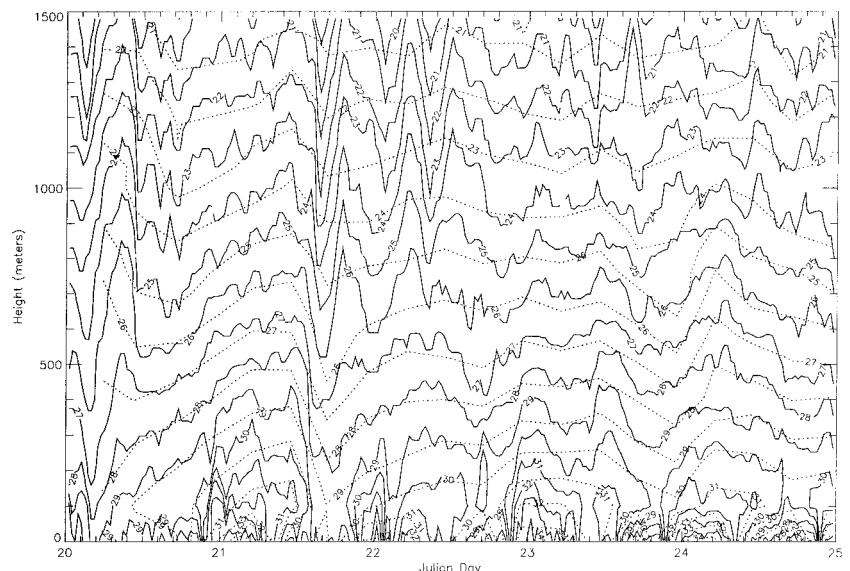


FIG. 11. Time-height cross sections of RASS-derived virtual temperature for the period 20–25 January 1993 in Kavieng, PNG. The dashed contours were derived from the 6-hourly radiosonde data.

height cross sections of T_v for the period 20–25 January. For comparison, we have superimposed the corresponding contours (dashed lines) drawn using the radiosonde data. There is clear variation of T_v on temporal scales less than 6 h. Two features are of note: the sudden coolings at about Julian times 20.25 and 21.5 were associated with rain. Clearly seen also is the solar heating during the days (sunup occurs at 2000 UTC and sundown occurs at 0800 UTC). However, nothing in the T_v behavior reflects the sudden drying that occurs on 23 January.

e. FTIR

One of our primary objectives during PROBE was to compare measured and calculated values of spectral radiance during clear conditions. Unfortunately, completely clear conditions were infrequent. To find clear cases, we used a combination of optical and infrared irradiance data, as well as the occasional periods when the cloud lidar was operating. In all, we found six clear cases in which the FTIR was operating and a radiosonde launch occurred within 1 h. Figure 12 shows an example of measured radiance and that calculated from the LBLRTM. We note that in the

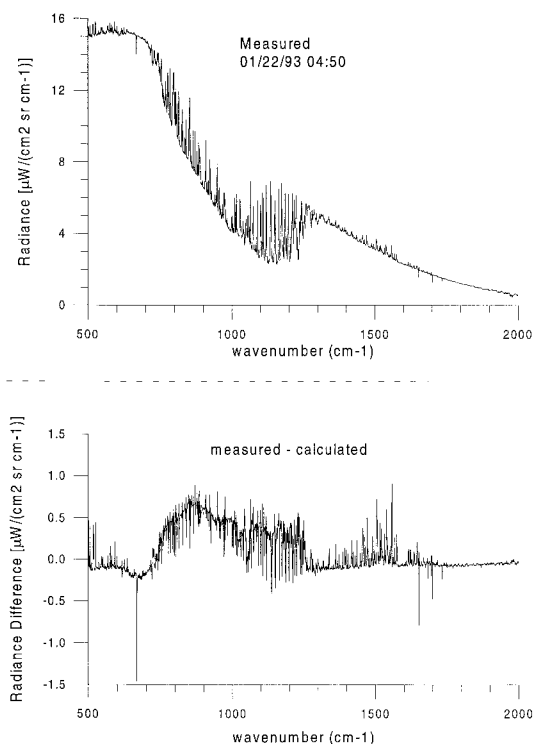


FIG. 12. (a) Measured FTIR spectra, Kavieng, PNG, 0450 UTC 22 January 1993. (b) Difference between measured and calculated spectra. Spectra calculated by LBLRTM (Clough et al. 1992) based on the 0500 UTC CLASS radiosonde launch.

water vapor window region (830 to 1250 cm^{-1}), the calculations are lower than measurements by about 5%. These measurements were used to update the Clough–Kniezys–Davis (CKD) continuum formulation (Clough et al. 1989; Clough et al. 1992) and the adjustments were verified by subsequent measurements (Han et al. 1997).

We show in Fig. 13 measured infrared radiance during known (from MWSR observations) cloud liquid conditions (see section 3), including two liquid clouds, and two clear conditions during which there were substantial differences in PWV. The spikes in the spectra below about 700 cm^{-1} and beyond about 1400 cm^{-1} are associated with calibration uncertainties at strong absorption lines. However, the structure in the spectra from about 800 to 1300 cm^{-1} is associated with water vapor and ozone absorption. Notice that the two clear cases [(a) and (b) in Fig. 13] are substantially different in the window region. Case spectrum (a) in Fig. 13 was taken during the driest portion of the drying event while Case spectrum (b) represents the situation when the PWV had recovered to an average value. Thus the drying event is clearly discernable in the high-resolution FTIR spectra. Case spectra (c) and (d) show integrated cloud liquid amounts of 0.046 and 0.080 mm, respectively. Together with the PWV of 5.18 cm, the ICL of 0.08 mm is enough to make the Case (d) spectrum resemble that from a blackbody. We also observed that the infrared radiance from cirrus clouds, which shows so clearly in drier environments in the infrared win-

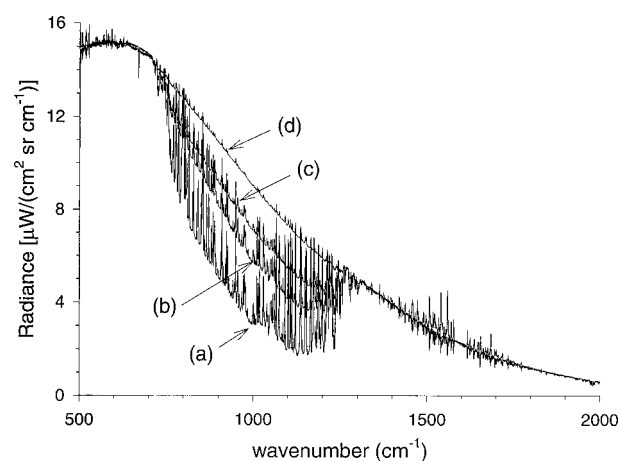


FIG. 13. FTIR spectra of infrared radiance taken at Kavieng, PNG, 22, and 23 January 1993: (a) PWV = 3.9 cm, ICL = 0.0 mm; (b) PWV = 5.6 cm, ICL = 0.0; (c) PWV = 5.6 cm, ICL = 0.046 mm; and (d) PWV = 5.2 cm, ICL = 0.08 mm. The 10-min averages of PWV and ICL were obtained from the MWSR.

dow region for 833 to 1250 cm^{-1} , is difficult to identify in the moist tropical atmosphere at Kavieng. Earlier observations taken at Coffeyville, Kansas, for a variety of cloud conditions, when the water vapor was in the 1 – 2 -cm range, showed brightness temperature contrasts of the order of 150 K between clear and cloudy conditions.

f. MWSR observations of cloud liquid

The amount of ICL was derived from the two channels of the MWSR, again using linear statistical inversion using the two derived optical depths as components of the data vector (Westwater 1993). The complete time series of derived ICL during 20 January–28 February 1993, is shown in Fig. 14. Here, we have eliminated observations for which the inferred ICL is greater than 10 mm , corresponding to a $31.65\text{ GHz } T_b$ of about 250 K , as well as the outliers that are shown in Fig. 4. It is obvious from the time series that substantial amounts of cloud liquid (and rain) frequently occur. The frequency distribution of ICL, for inferred ICL

greater than 0.04 mm , is shown in Fig. 15. If we use the 0.04 mm as the boundary between clear and (liquid) cloudy conditions, then measurable ICL occurred 44% of the time. As shown by Snider and Hazen (1998), this frequency distribution differs considerably from nontropical observations. For example, for 3.6% of the observations ICL exceeds 3 mm , whereas at higher latitudes, ICL exceeds this level, usually less than 1% of the time. We examined the frequency of occurrence of ICL amounts and because of the success in predicting rain statistics using a lognormal distribution (Crane 1996), we tried applying similar modeling to our ICL distributions. As shown in Fig. 15, our fit to these data works quite well, and it is convincing that our assumption of a log normal distribution is justified over this range (0.04 – 10.0 mm) of ICL.

4. Summary and discussion

During phase two of PROBE, about six weeks of continuous measurements of PWV and ICL were obtained. During this time, about 1700 FTIR spectra were also obtained. Initial comparisons of microwave radiometric data with CLASS radiosondes indicate rms agreement of about 6% (0.31 cm rms) in PWV. The differences between MWSR retrievals and radiosonde measurements of PWV could have been caused by lot-dependent calibration batches of radiosondes. For long periods of time, say two weeks, the radiometer and

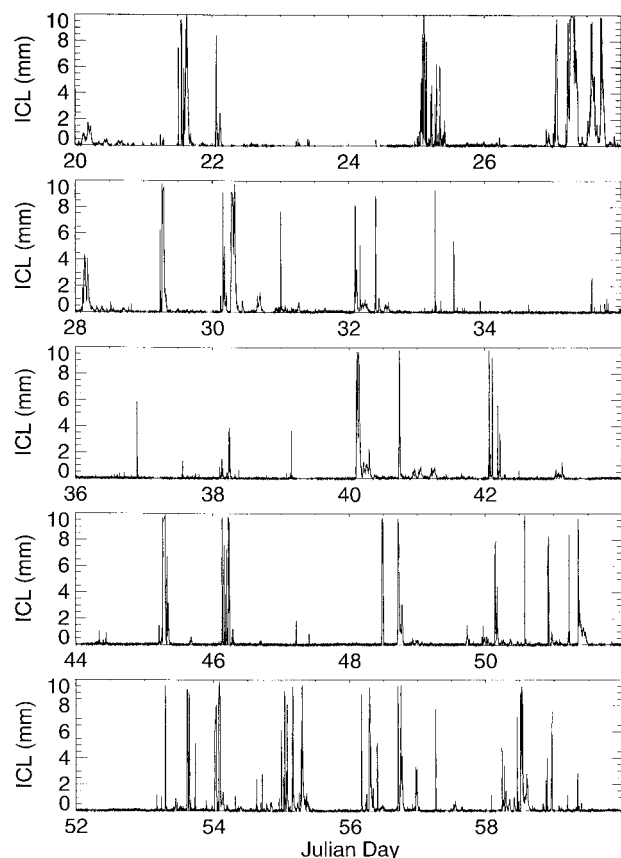


FIG. 14. Time series of ICL derived from MWSR at Kavieng, PNG, 14 January–28 February 1993. Data larger than 10 mm have been removed from the analysis. Times are in Julian day (UTC).

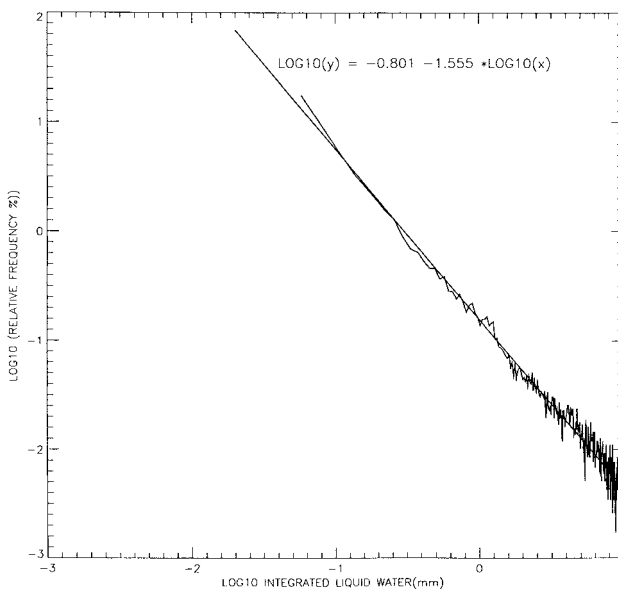


FIG. 15. Frequency distribution of ICL obtained from the data shown in Fig. 14.

radiosonde data would track each other closely and then the two sets of measurements would diverge by as much as 5 mm. Extensive examination into the internal and external calibration characteristics of the radiometer showed no apparent change. It is strongly recommended that in further such experiments the calibration lot numbers of the radiosondes be archived so that the calibration can be traced back to the manufacturer's calibration.

Presumably because of the effects of solar heating on horizontal stratification and because of frequent occurrence of clouds, the standard method of calibration of the MWSR by the tip cal method was not entirely satisfactory, since only a small number of useable tip calcs were achievable. This lack was in part due to security considerations in which nighttime operations were not recommended. Certainly for the unattended deployment of microwave radiometers in the tropical western Pacific as is occurring for the Department of Energy's ARM program (Stokes and Schwartz 1994), continuous tip cal scanning is recommended to increase the number of useable tip calcs. A continuously operating cloud lidar capable of measuring cloud base heights to at least 5 km would also be of substantial benefit in determining the occurrence of liquid-bearing clouds.

For the only unambiguously clear sounding that we obtained when the FTIR was operating close to a radiosonde release time and the PWV derived from the MWSR agreed with that from the radiosonde, LBLRTM calculations were lower than measurements in the window region, indicating that some adjustments to water vapor continuum calculations were required. These measurements were used to update the CKD continuum formulation (Clough et al. 1992) and the adjustments were verified by subsequent measurements (Han et al. 1997). The use of a microwave radiometer to check both the radiosonde quality and temporal representativeness allowed such quality FTIR measurement to be made. Observations of infrared radiance were also made during the presence of both liquid-bearing and cirrus clouds. Because of the substantial attenuation by water vapor, the influence of cirrus clouds on downwelling radiance observed at the surface is much less than in midlatitude observations. For this reason, to unambiguously determine if the radiance observed by an FTIR is from clear skies only, a high quality lidar, probing to perhaps tropopause altitudes, is necessary.

We examined in detail an event in which substantial drying occurred over the PROBE site. The ground-

based PWV observations by both the MWSR and radiosondes were in close quantitative agreement during this time. Interpretation of the event was substantially aided by wind profiler measurements and SSM/I images of PWV, which were consistent with the picture of a relatively dry mass of air being advected over the site by the prevailing winds. This dry episode was accompanied by a substantial decrease in cloudiness over the site, which had a significant effect on the surface radiative budget, yet little effect on the top-of-atmosphere radiative energy budget. This, in turn, implies that a repartitioning of the radiative heating between the surface and atmospheric column was occurring. The drying event was also clearly evident in the window region of the FTIR spectra. We also examined the RASS soundings of virtual temperature during this event and found no discernable effect.

An almost continuous time series of cloud liquid water was also obtained and a probability distribution of ICL was obtained. If an ICL threshold of 0.04 mm is chosen to divide clear and cloudy conditions, then liquid clouds occurred 44% of the time. Not surprisingly, substantial differences occur between ICL distributions observed during PROBE and those observed at other latitudes. The frequency distribution was well described by a lognormal distribution over the ICL range of 0.04 to 10.0 mm. Such a distribution might be useful in modeling, for example, the probability distribution of solar radiation that has been modulated by liquid clouds. Such distributions have been constructed from SSM/I data, but only up to four samples per day are available, and the horizontal footprint is of the order of 25 km. The data presented here, as derived from the MWSR, have high temporal resolution (30 s), a horizontal resolution of about 90 m at 1 km distance, and an estimated accuracy of the liquid retrievals of 15%. An instrument of this type will be deployed in the tropical western Pacific on the R/V *Ron Brown* in the summer of 1999 as a part of the NAURU'99 deployment.

All of the microwave and infrared radiometric data; the ISS radiosonde, surface, and remote sensing data; as well as the long- and short-surface radiation data are available at the Pennsylvania State University Web site (http://aero.essc.psu.edu/pub/data5/togacoare_site/L4/)

Acknowledgments. The work presented in this paper was sponsored by the Environmental Sciences Division of the Department of Energy as a part of their Atmospheric Radiation Measurement program. The authors thank Drs. R. S. Sheu and G. Liu for provid-

ing processed SSM/I data. In addition, the authors acknowledge useful comments on the manuscript by S. A. Clough and P. May.

References

- Angevine, W. M., W. L. Ecklund, D. A. Carter, K. S. Gage, and K. P. Moran, 1994: Improved radio-acoustic sounding techniques. *J. Atmos. Oceanic Technol.*, **11**, 42–49.
- Berk, A., L. S. Bernstein, and D. C. Robertson, 1989: Modtran: A Moderate Resolution Model for LOWTRAN 7. Air Force Geophysics Laboratory Rep. GL-TR-89-0122, 38 pp.
- Carter, D. A., K. S. Gage, W. L. Ecklund, W. M. Angevine, P. E. Johnston, A. C. Riddle, J. Wilson, and C. R. Williams, 1995: Developments in UHF lower tropospheric wind profiling at NOAA's Aeronomy Laboratory. *Radio Sci.*, **30**, 977–1001.
- Clough, S. A., F. X. Kneizys, and R. W. Davies, 1989: Line shape and the water vapor continuum. *Atmos. Res.*, **23**, 229–241.
- , M. J. Iacono, and J.-L. Moncet, 1992: Line-by-line calculation of atmospheric fluxes and cooling rates: Application to water vapor. *J. Geophys. Res.*, **97**, 15 761–15 785.
- Cole, H., and E. Miller, 1995: A correction for low-level radiosonde temperature and relative humidity measurements. Preprints, *Ninth Symp. on Meteorological Observations and Instrumentation*, Charlotte, NC, Amer. Meteor. Soc., 32–36.
- Crane, R. K., 1996: *Electromagnetic Propagation through Rain*. John Wiley and Sons, 273 pp.
- Han, Y., and E. R. Westwater, 1995: Remote sensing of tropospheric water vapor and cloud liquid water by integrated ground-based sensors. *J. Atmos. Oceanic Technol.*, **12**, 1050–1059.
- , J. B. Snider, E. R. Westwater, S. H. Melfi, and R. A. Ferrare, 1994: Observations of water vapor by ground-based microwave radiometers and Raman lidar. *J. Geophys. Res.*, **99**, 18 695–18 702.
- , J. A. Shaw, J. H. Churnside, P. D. Brown, and S. A. Clough, 1997: Infrared spectral measurements in the tropical Pacific atmosphere. *J. Geophys. Res.*, **102**, 4353–4356.
- Hogg, D. C., F. O. Guiraud, J. B. Snider, M. T. Decker, and E. R. Westwater, 1983: A steerable dual-channel microwave radiometer for measurement of water vapor and liquid in the troposphere. *J. Appl. Meteor.*, **22**, 789–806.
- Liebe, H. J., 1989: MPM, An atmospheric millimeter wave propagation model. *Int. J. Infrared Millimeter Waves*, **10**, 631–650.
- , and D. H. Layton, 1987: Millimeter wave properties of the atmosphere: Laboratory studies and propagation modeling. National Telecommunications and Information Administration (NTIA) Rep. 87-24, 74 pp. [Available from National Technical Information Service, Springfield, VA 22161.]
- Liljegren, J. C., and B. M. Lesht, 1996: Measurements of integrated water vapor and cloud liquid water from microwave radiometers at the DOE ARM Cloud and Radiation Testbed in the U.S. Southern Great Plains. *Proc. Int. Geophysics and Remote Sensing Symp. '96*, Lincoln, NB, IEEE, 1675–1677.
- Long, C. N., 1996: Surface radiative energy budget and cloud forcing: Results from TOGA COARE and techniques for identifying and calculating clear sky irradiance. Ph.D. dissertation. The Pennsylvania State University, 193 pp.
- , and T. P. Ackerman, 1997: Detection of clear skies using total and diffuse SW irradiance: Calculations of SW cloud forcing and clear-sky diffuse ratio. *Proc. Sixth Atmospheric Radiation Measurement (ARM) Science Team Meeting*, San Antonio, TX, Dept. of Energy, 179–183.
- , ——, D. S. Renné, J. M. Hacker, A. G. Williams, and E. R. Westwater, 1994: Surface radiative energy budget and radiative instrument inter-comparison from the ARM PROBE Project, Preprints, *Eighth Conf. on Atmospheric Radiation*, Nashville, TN, Amer. Meteor. Soc., 169–171.
- May, P. T., R. G. Strauch, K. P. Moran, and W. L. Ecklund, 1990: Temperature sounding by RASS with wind profiling radars: A preliminary study. *IEEE Trans. Geosci. Remote Sens.*, **28**, 19–28.
- Parsons, D., and Coauthors, 1994: The Integrated Sounding System: Description and preliminary observations from TOGA COARE. *Bull. Amer. Meteor. Soc.*, **75**, 553–567.
- Platt, C. M. R., S. A. Young, P. J. Manson, G. R. Patterson, S. C. Marsden, R. T. Austin, and J. Churnside, 1998: The optical properties of equatorial cirrus from observations in the ARM Pilot Radiation Observation Experiment. *J. Atmos. Sci.*, **55**, 1977–1996.
- Renné, D. S., T. A. Ackerman, and W. E. Clements, 1994: PROBE: The Pilot Radiation Observation Experiment. Preprints, *Eighth Conf. on Atmospheric Radiation*, Nashville, TN, Amer. Meteor. Soc., 270–271.
- Riddle, A. C., W. M. Angevine, W. L. Ecklund, E. R. Miller, D. B. Parsons, D. A. Carter, and K. S. Gage, 1996: In situ and remotely sensed horizontal winds and temperature intercomparisons obtained using Integrated Sounding System during TOGA COARE. *Contrib. Atmos. Phys.*, **69**, 49–61.
- Shaw, J. A., J. H. Churnside, and E. R. Westwater, 1991: An infrared spectrometer for ground-based profiling of atmospheric temperature and humidity. *Proc. SPIE Int. Symp. on Optical Appl. Sci. and Engineering*, San Diego, CA, SPIE, 681–686.
- Sheu, R.-S., and G. Liu, 1995: Atmospheric humidity variations associated with westerly wind bursts during TOGA COARE. *J. Geophys. Res.*, **100**, 25 759–25 768.
- Snider, J. B., and D. A. Hazen, 1998: Surface-based radiometric observations of water vapor and cloud liquid in the temperate zone in the tropics. *Radio Sci.*, **33**, 421–432.
- Stokes, G. M., and S. E. Schwartz, 1994: The Atmospheric Radiation Measurement (ARM) program: Programmatic background and design of the Cloud and Radiation Testbed. *Bull. Amer. Meteor. Soc.*, **75**, 1201–1221.
- Toon, O. B., C. P. McKay, T. P. Ackerman, and K. Santhanam, 1989: Rapid calculation of radiative heating rates and photodissociation rates in inhomogeneous multiple-scattering atmospheres. *J. Geophys. Res.*, **94**, 16 287–16 301.
- Webster, P. J., and R. Lucas, 1992: TOGA COARE: The Coupled Ocean–Atmosphere Response Experiment. *Bull. Amer. Meteor. Soc.*, **73**, 1377–1416.
- Westwater, E. R., 1993: Ground-based microwave remote sensing of meteorological variables. *Atmospheric Remote Sensing by Microwave Radiometry*, M. Janssen, Ed., John Wiley and Sons, 145–213.
- Wilson, W. H., 1980: Solar ephemeris algorithm. Scripps Institution of Oceanography Rep. SIO-80-13, 73 pp. [Available from Technical Publications, Scripps Institution of Oceanography, 9500 Gilman Drive, Dept. 0233, La Jolla, CA 92093-5306.]